

Electron momentum-space densities and Fermi surface of $\text{Li}_{100-x}\text{Mg}_x$ ($0 \leq x \leq 40$) alloys: Compton scattering experiment versus theory

G. Stutz,* F. Wohlert, A. Kaprolat, and W. Schülke
Institute of Physics, University of Dortmund, D-44221 Dortmund, Germany

Y. Sakurai and Y. Tanaka
The Institute of Physical and Chemical Research, Wako, Saitama 351-01, Japan

M. Ito
Faculty of Science, Himeji Institute of Technology, Kamigohri, Hyogo 678-12, Japan

H. Kawata
Photon Factory, National Laboratory for High Energy Physics, Tsukuba, Ibaraki 305, Japan

N. Shiotani
Tokyo University of Fisheries, Kounan, Minato, Tokyo 108, Japan

S. Kaprzyk[†] and A. Bansil
Department of Physics, Northeastern University, Boston, Massachusetts 02115
 (Received 4 January 1999)

Directional Compton profiles (CP's) of $\text{Li}_{100-x}\text{Mg}_x$ ($0 \leq x \leq 40$) were measured for (11)12 directions of the momentum transfer \mathbf{q} with (0.14) 0.16 a.u. (a.u.=atomic units: $\hbar = e = m = 1$) momentum space resolution using synchrotron x rays, monochromatized to (31) 59 keV (values in brackets refer to $x=0$). The total experimental valence electron CP's, their second derivatives, and the associated directional differences were compared with the corresponding Korringa-Kohn-Rostoker-coherent-potential-approximation-local-density-approximation (KKR-CPA-LDA) computations. Discrepancies between measurements and calculations are partly traced back to an inadequate treatment of electron correlation effects within the LDA framework. The three-dimensional (3D) valence-electron momentum density, $\rho(\mathbf{p})$, as well as the 3D occupation number density $N(\mathbf{k})$, were reconstructed from experimental data using the Fourier-Bessel method. The reconstructed $\rho(\mathbf{p})$'s exhibit evidence of higher momentum components due to 110 umklapp processes, whose variations with x are in reasonable agreement with the KKR-CPA calculations. The experimental $N(\mathbf{k})$'s provide a direct measure of the Fermi-surface anisotropy and show the presence of necks on the 110 Brillouin-zone boundaries for $x \geq 13$ in good accord with 2D positron annihilation experiments. [S0163-1829(99)14833-1]

I. INTRODUCTION

$\text{Li}_{100-x}\text{Mg}_x$ alloys form a solid solution of Mg in the bcc Li lattice¹ over a wide range of composition $0 < x < 70$; the average number of valence electrons per atom then varies continuously from 1 to 1.7, while the lattice constant increases only slightly from 6.633 a.u. (a.u.=atomic units: $\hbar = e = m = 1$) to 6.648 a.u. with a shallow minimum of 6.603 a.u. at $x = 35$.² Insofar as the Fermi surface (FS) is concerned, we expect the nearly free-electron FS of Li to expand with increasing Mg content and make contact with the Brillouin-zone (BZ) boundary first along the direction of the shortest reciprocal-lattice vector (\mathbf{G}_{110} for bcc) at a certain critical concentration x_c (48% Mg for the free-electron model). For these reasons, LiMg alloys have been the subject of numerous experimental studies to test theoretical models of electronic structure of chemically disordered solids. In this vein, we have been motivated to undertake the present study since the Compton spectra provide a direct measure of the ground-state electron momentum density and hence of the underlying electronic wavefunctions and the FS.

Recent work^{3,4} has shown that directional Compton profiles (CP's) with a momentum space resolution of the order of 0.1 a.u. can yield useful information about the electron momentum density including its higher momentum components arising from umklapp processes. Additionally, quite small anisotropies associated with the asphericity of the FS can be deduced. This is especially important for testing band theory predictions since the conventional FS technique of choice, the de Haas-van Alphen (dHvA) effect, is not applicable in this case. The reason is that the bcc Li undergoes a martensitic transition to a mixed bcc/9R samarium-like phase for $T < 75$ K,⁵ so that the low temperatures needed for carrying out dHvA measurements are not feasible. Notably Randles and Springford⁶ approached the problem by artificially suppressing the martensitic transition by measuring dHvA in a polycrystalline dispersion of Li spheres of small size; the directional information was of course lost in this way. On the other hand, the Compton scattering⁷ and angular correlation of positron annihilation radiation⁸ (ACAR) experiments do not require long mean free paths or low temperatures and, therefore, are especially suited to study the

bcc LiMg alloys. Relative to ACAR, the Compton technique possesses the advantage that the interpretation of the spectra is not complicated by the presence of the positron. In particular, backfolding of the momentum density into the first BZ either by utilizing the Lock-Crisp-West (LCW) theorem⁹ or the corresponding Fourier theorem of Schülke,¹⁰ strictly yields the occupation number density only in the case of Compton scattering and not of ACAR spectra.

It should be noted that in disordered alloys of interest to this paper, another effect comes into play in inducing finite electronic lifetimes, namely, the disorder scattering of states. Consequently, even at low temperatures, the application of the dHvA and other techniques based on transport phenomena is generally limited to the dilute impurity regime. By contrast, the Compton and ACAR experiments are applicable to concentrated alloys. In comparing Compton and ACAR, we should also keep in mind that the two spectroscopies probe the electronic structure differently.

The positron can show a preferential affinity for a specific site in a binary alloy, whereas the Compton would sample the electronic states more uniformly. Indeed, a difference in the positron affinity between Li and Mg sites has been predicted in LiMg alloys¹¹ due to differences in the associated pseudopotentials.¹² Early one-dimensional (1D) ACAR study of polycrystalline LiMg samples was reported by Stewart.¹³ Refs. 11 report 1D-ACAR and positron lifetime measurements, also on polycrystals, with focus on the issue of positron affinity, but find no indication of preferential annihilation for $x < 50$. References 14 undertake a combined 1D-ACAR and Compton study and discuss their results mainly in terms of blurring of the FS due to disorder scattering; the FS contact with the 110-BZ boundary was estimated to occur between 30 and 40 at. % Mg, although FS information could only be obtained indirectly since polycrystalline samples were used. A detailed 2D-ACAR FS study of Li and LiMg alloys has been carried out by Triftshäuser *et al.*¹⁵ and the results analyzed in terms of charge selfconsistent Korringa-Kohn-Rostoker coherent-potential approximation (KKR-CPA) computations based on the local-density approximation (LDA) by Rajput *et al.*¹⁶ By utilizing a scheme for reconstructing the occupation number density via LCW folding, Ref. 16 obtains details of the FS anisotropy for $0 \leq x \leq 60$. KKR-CPA calculations predict FS contact along the 110 direction to occur at $x_c = 17 \pm 4$ (where the FS radius is defined as the position of the peak in the spectral density function in the alloy). This result is in reasonable accord with the value of $x_c = 20$ deduced from thermopower and resistivity measurements,¹⁷ and $x_c = 24.7$ calculated by Vaks *et al.*,¹⁸ but in disagreement with Hall voltage,¹⁹ optical,²⁰ and Knight shift²¹ experiments, all of which deduce x_c values larger than 30. x_c was difficult to deduce accurately in the ACAR work of Ref. 16 since the data was taken only for $x \geq 28$.

Bearing these considerations in mind, it seemed worthwhile to undertake a theory-experiment study of LiMg alloys. With the more direct access to the electron momentum density and FS's provided by the high-resolution Compton scattering technique, we decided to confront highly accurate parameter free KKR-LDA-CPA computations with the corresponding measurements for a range of alloy compositions. A fairly large number of directional CP's for each composi-

tion have been measured as well as computed in order to carry out a proper 3D reconstruction of the momentum space and occupation number densities. The fact that a Compton experiment involves a 1D projection of the 3D momentum density and a concomitant loss of information is ameliorated via measurements along many directions in this manner, as has been demonstrated previously in the study of pure Li.⁴

The remainder of this paper is organized as follows: In Sec. II some basic relations which connect Compton profiles both with the electron momentum space density and the occupation number density are outlined in order to clarify the reconstruction of these quantities. Section III gives salient details of the KKR-LDA-CPA computations. Section IV gives the relevant details of experiments and data processing. In Sec. V the experimental results in the form of (i) directional CP differences, (ii) reconstructed electron momentum space densities, (iii) reconstructed occupation number densities and FS anisotropy, and (iv) second derivatives of the CP's are presented and compared with the corresponding theoretical quantities. Finally, Sec. VI outlines the conclusions of this study.

II. BASIC RELATIONS

Under the conditions of the impulse approximation,²² the double differential cross section for inelastic scattering from an electron system, as measured in a Compton scattering experiment, is proportional to the so-called Compton profile $J(p_z)$:²³

$$d^2\sigma/d\omega_2 d\Omega = C(\omega_1, \omega_2, p_z)J(p_z), \quad (1)$$

where ω_1 and ω_2 are the frequencies of the incoming and scattered beam, respectively. p_z , which is the component of the electron momentum in the direction of the momentum transfer \mathbf{q} , is connected with the variables of the Compton scattering experiment by

$$p_z = mc[\hbar\omega_1 - \hbar\omega_2 - (\hbar^2\omega_1\omega_2/mc^2) \times (1 - \cos\phi)] / [(\hbar^2\omega_1^2 + \hbar^2\omega_2^2 - 2\hbar^2\omega_1\omega_2\cos\phi)^{1/2}], \quad (2)$$

where ϕ is the scattering angle.

The Compton profile $J(p_z)$ contains the desired information about momentum space density of the scattering system via

$$J(p_z) = \int \int \rho(\mathbf{p}) dp_x dp_y, \quad (3)$$

where $\rho(\mathbf{p})$ is the electron momentum density which can be written in terms of one-electron Bloch states, labeled by the reduced wave vector \mathbf{k} and band index ν , as follows:

$$\rho(\mathbf{p}) = \sum_{\nu, \nu'} \sum_{\mathbf{k}} \sum_{\mathbf{G}} n_{\nu\nu'}(\mathbf{k}) a_{\nu}^*(\mathbf{k} + \mathbf{G}) a_{\nu'}(\mathbf{k} + \mathbf{G}) \times \delta(\mathbf{k} + \mathbf{G} - \mathbf{p}/\hbar), \quad (4)$$

where $n_{\nu\nu'}(\mathbf{k})$ is the occupation number density, whose off-diagonal elements shall be neglected in what follows, an approximation, which was shown to be justified for nearly-free-electron metals by Lundqvist and Lyden.²⁴ Accordingly, we

skip the double summation ν, ν' in the following. $a_\nu(\mathbf{k} + \mathbf{G})$ are plane-wave expansion coefficients of the Bloch-type wave function $\psi_{\mathbf{k},\nu}(r)$, where \mathbf{G} are reciprocal-lattice vectors:

$$N(\mathbf{k}) \equiv \sum_\nu n_\nu(\mathbf{k}) \quad (5)$$

contains the desired information about the Fermi surface, whereas $\rho(\mathbf{p})$ reflects the distribution of higher momentum components via $|a_\nu(\mathbf{k} + \mathbf{G})|^2 \delta(\mathbf{k} + \mathbf{G} - \mathbf{p}/\hbar)$ with $\mathbf{G} \neq \mathbf{G}_\nu$, where \mathbf{G}_ν characterizes the ν th band in an empty-lattice extended zone scheme.

The 3D reconstruction of $\rho(\mathbf{p})$ and $N(\mathbf{k})$ are performed by utilizing the properties¹⁰ of the so-called reciprocal form factor²⁵ defined by

$$B(\mathbf{r}) = \int d^3p \rho(\mathbf{p}) \exp(-i\mathbf{p} \cdot \mathbf{r}). \quad (6)$$

In view of Eq. (3), $B(0,0,z)$ can be obtained from the 1D Fourier transform of the measured Compton profiles:

$$B(0,0,z) = \int J(p_z) \exp(-ip_z z) dp_z. \quad (7)$$

As shown in Ref. 4, the complete $B(\mathbf{r})$ function and, via a back transformation the $\rho(\mathbf{p})$, can be obtained by expanding $B(\mathbf{r})$ into lattice harmonics and by least-square fitting the expansion coefficients to the experimental $B(0,0,z)$ data from directional CP's (so-called Fourier-Bessel method²⁶). Finally, one can use this complete 3D $B(\mathbf{r})$ function to reconstruct the occupation number density $N(\mathbf{k})$ using the Fourier series¹⁰

$$N(\mathbf{k}) = (V_0/8\pi^3) \sum_{\mathbf{R}} B(\mathbf{R}) \exp(-i\mathbf{k} \cdot \mathbf{R}), \quad (8)$$

where V_0 is the volume of the elementary cell and \mathbf{R} is a lattice translation vector. The issue of propagation of statistical error in the reconstructed $\rho(\mathbf{p})$ and $N(\mathbf{k})$ is discussed in detail in Ref. 4.

III. KKR-LSD-CPA CALCULATIONS

The Compton profile (CP) calculations in $\text{Li}_{100-x}\text{Mg}_x$ were carried out within the all-electron charge self-consistent KKR-LSD-CPA framework and are parameter free, the use of LDA for treating exchange-correlation effects and the KKR-CPA for the disorder effects notwithstanding. In this work, total energies were not minimized to determine the lattice constant at each concentration, but instead the experimental lattice data were used. The result for the limiting case of $x=0$ are in good agreement with those obtained independently in Li via the KKR approach. The electronic structure and Fermi surface of $\text{Li}_{100-x}\text{Mg}_x$ using the same methodology has been reported previously in Ref. 16. The underlying KKR-LSD-CPA methodology is described in Refs. 27–29; the relevant Green's-function formulation for treating the momentum density and CP's in disordered alloys is given in Refs. 30–32. The exchange-correlation effects have been incorporated within the von Barth-Hedin local-spin density (LSD) approximation.³³ The Lam-Platzman correction³⁴ for

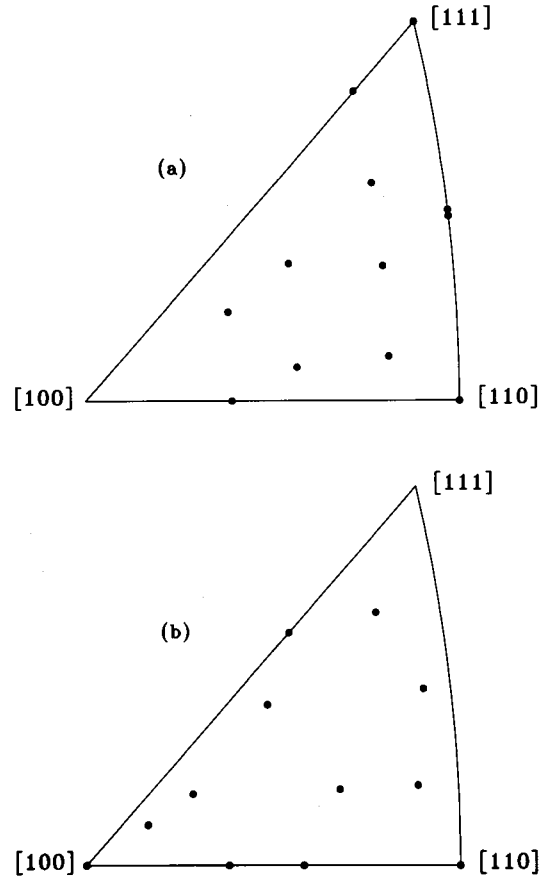


FIG. 1. Irreducible orientation triangles of cubic symmetry; measured \mathbf{q} directions are represented by points; (a) $\text{Li}_{60}\text{Mg}_{40}$; (b) $\text{Li}_{87}\text{Mg}_{13}$, and $\text{Li}_{72}\text{Mg}_{28}$.

Li was computed using the occupation number density for the uniform electron gas; a similar correction for the case of LiMg alloy was not computed since the procedure for such a calculation is somewhat unclear in alloys and, in any event, these corrections being spherically symmetric induce spurious structure in the CP at the free-electron Fermi radius.

Concerning technical details, the crystal potential in $\text{Li}_{100-x}\text{Mg}_x$ for $x=0, 13, 28, 40$ was obtained by iterating the KKR-CPA cycles using an elliptical contour with 48 energy points in the complex energy plane. The final Li and

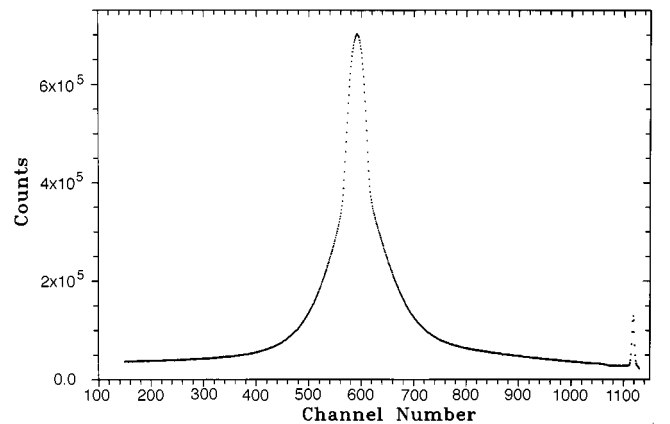


FIG. 2. A typical raw Compton spectrum. The profile of $\text{Li}_{60}\text{Mg}_{40}$ for $\mathbf{q} \parallel [110]$ is shown.

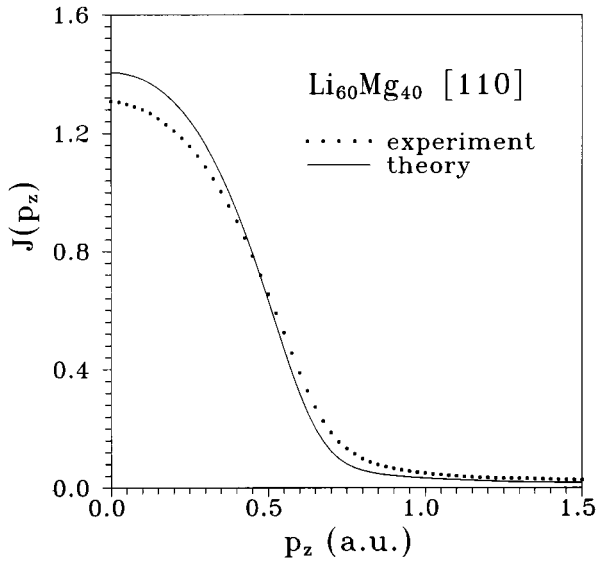


FIG. 3. A typical valence-electron CP. Results for $\text{Li}_{60}\text{Mg}_{40}$ for $\mathbf{q} \parallel [110]$ are shown. Points indicate the experiment; solid line indicates the KKR-CPA calculation.

Mg charge densities for each alloy composition considered are self-consistent to an accuracy of about 10^{-4} electrons/atom and the Fermi energies to 10^{-4} Ry. A maximum angular momentum cutoff of $l_{\text{max}}=2$ was employed in all cases.

In order to obtain the CP, the 3D momentum density $\rho(\mathbf{p})$ was first evaluated in terms of the momentum matrix element of the KKR-CPA Green's function²⁹⁻³¹ over a fine mesh of $48 \times 1785 \times 177$ \mathbf{p} points covering momenta up to $p_{\text{max}}=5$ a.u. This mesh involves 1785 \mathbf{k} points in the 1/48th irreducible part of the Brillouin zone with each \mathbf{k} point translated into 177 \mathbf{p} points by adding reciprocal-lattice vectors; the factor of 48 accounts for the symmetry operations of the cubic point group. The CP can then be computed by evaluating the 2D integrals of Eq. (3) accurately. The final CP's have been calculated over a momentum mesh containing 201 \mathbf{p} points in the range 0-3 a.u. along each of the 11 measured directions in Li and 12 directions each for the three alloy compositions. The accuracy of the present CP's is about 1 part in 10^4 .

IV. EXPERIMENT AND DATA PROCESSING

The Compton measurements on the LiMg alloys were performed at the Compton spectrometer installed at the NE1-beamline of the KEK-accumulation ring operated at 6.4 GeV and 35-20 mA. The x-ray source of this beamline is an electromagnetic 41-pole wiggler with a critical photon energy of 26.5 keV. The double focusing Si(111) monochromator³⁵ consists of 20 independently adjustable Si crystal rods accepting a 155 mm wide horizontal opening of the beam over a length of 10 mm. Each of these rods is cylindrically bent for horizontal focusing, where segmentation prevents anticlassic bending. The vertical focusing can then be attained by an appropriate relative rotation of the rods with respect to an axis in the orbital plane perpendicular to the beam. This way the beam is focused to a spot of $3 \times 8 \text{ mm}^2$ on the sample, which is mounted in the scattering chamber of the Compton spectrometer, evacuated to 3

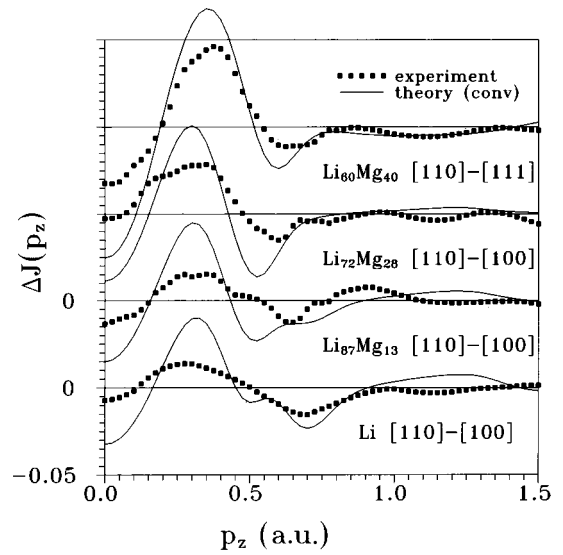


FIG. 4. Typical orientation differences of directional CP's. Results for [110]-[100] CP's of Li and LiMg alloys are shown; Points indicate the experiment; a Solid line indicates the resolution-broadened KKR (Li) and KKR-CPA (LiMg alloys) calculations.

$\times 10^{-6}$ mbar. The Compton spectrometer is described in detail elsewhere,³⁶ and consists of four independent analyzing systems arranged on the surface of a cone thus providing a scattering angle of 160° . Each analyzer is equipped with a triangular Cauchois-type Si(422) crystal cylindrically bent to a radius of 2.5 m, so that in each analyzing system a complete Compton spectrum was recorded on an image plate whose total spatial resolution was $200 \mu\text{m}$,³⁷ and whose efficiency with respect to uniformity and energy dependence was tested.³⁸ The image plates were read by a helium-neon-laser scanner with a $100 \times 100 \mu\text{m}^2$ focus. This way four directional CP's which differ with respect to the crystallographic orientation of the scattering vector \mathbf{q} could be measured simultaneously. The total momentum space resolution

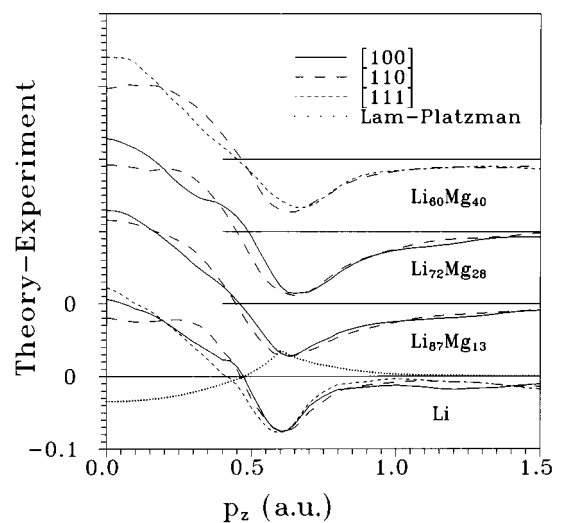


FIG. 5. Differences between calculated [(KKR-Li), KKR-CPA (LiMg alloys)] and measured directional valence-electron CP's for different \mathbf{q} orientations. The isotropic Lam-Platzman correction is shown on the Li results.

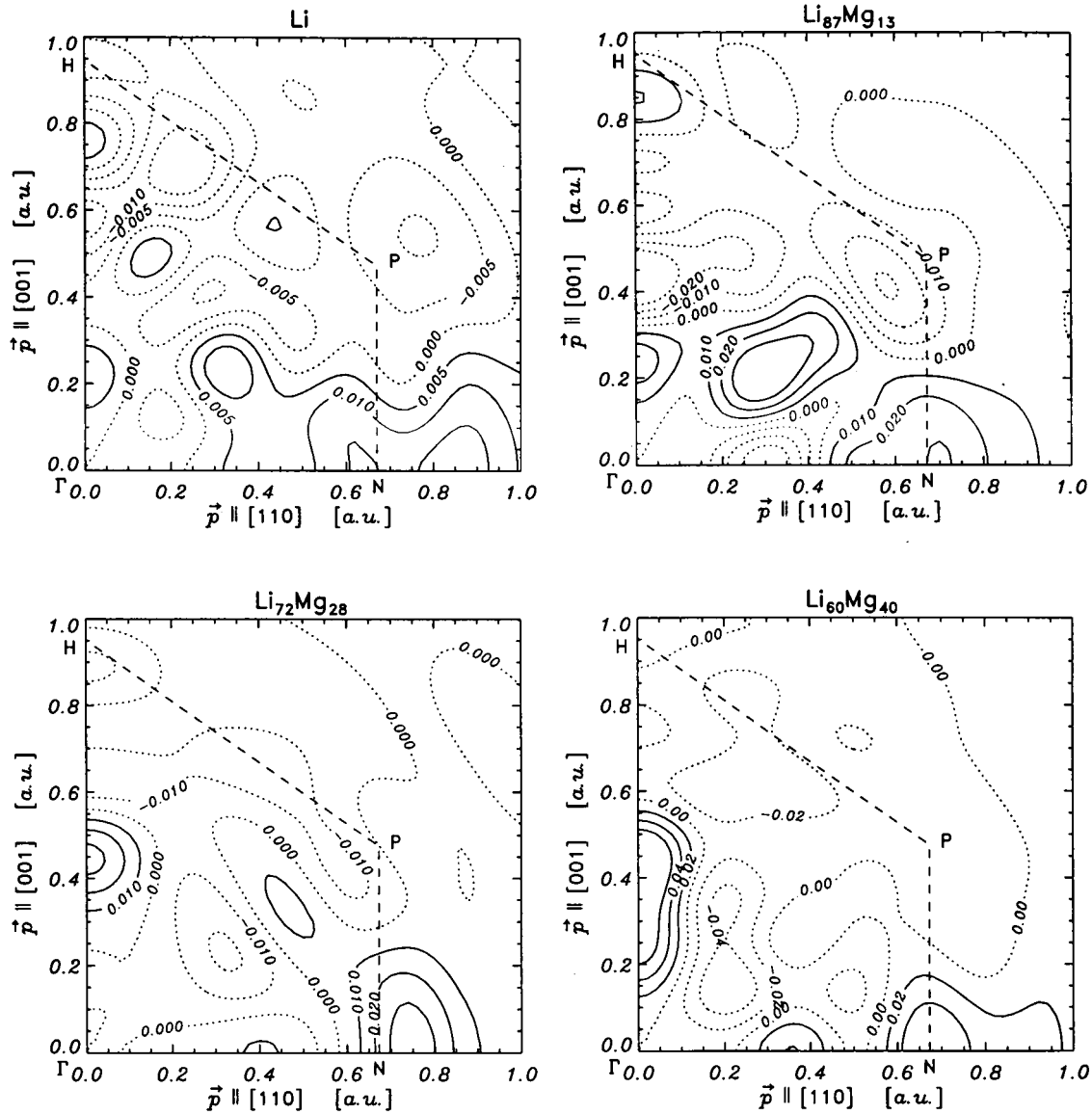


FIG. 6. Anisotropic parts $\Delta\rho(\mathbf{p})$ of the 3D valence-electron momentum densities reconstructed from the experimental CP's in Li and LiMg alloys are shown in the (110) plane as level diagrams. Solid lines are the positive values of $\Delta\rho(\mathbf{p})$; dotted lines are the negative values of $\Delta\rho(\mathbf{p})$; level-line distances are 0.005 a.u.^{-3} for Li, 0.01 a.u.^{-3} for $\text{Li}_{87}\text{Mg}_{13}$, and $\text{Li}_{72}\text{Mg}_{28}$; 0.02 a.u.^{-3} for $\text{Li}_{60}\text{Mg}_{40}$; dashed line is the BZ boundary.

of the Compton spectrometer is calculated³⁶ to be 0.11 a.u. and is determined mainly by the 88 eV bandwidth of the monochromator at the primary energy of 59.38 keV . However, the experimental resolution as measured by the width of the quasielastic line (see Fig. 2) varies; the best resolution is 0.145 a.u. which is found in the 40 at. \% Mg alloy specimen and the worst resolution is 0.173 a.u. , which is found in the 13 at. \% alloy specimen. The additional broadening is due to the fact that the final Compton spectrum is the result of adding up a large number of laser traces of the image plate by using the quasielastic peak as a guide. The weak quasielastic peak inevitably causes an extra broadening in this process, which decreases with increasing Mg content. In order to make comparison of experiment and theory easier we use a representative experimental resolution of 0.16 a.u. to convolute the theory.

The single-crystal $\text{Li}_{100-x}\text{Mg}_x$ samples with $x=13, 28,$

and 40 were grown by a modified Bridgman technique, and cut into plates of $1\text{--}3.5 \text{ mm}$ thickness perpendicular to $[110]$. The samples, which were stored in water-free paraffin oil, were cleaned from paraffin by heptan, then etched by a one-to-one mixture of methanol and 96% acetic acid and again cleaned with xylol. This entire chemical treatment was performed under Ar atmosphere within the scattering chamber, which was then immediately evacuated to $3 \times 10^{-6} \text{ mbar}$.

We have obtained 12 different Compton profiles for each LiMg alloy composition by measuring three different sample orientations in each case. The orientation distribution within the irreducible orientation triangle is shown in Fig. 1. In Fig. 2 a typical raw Compton spectrum is presented. For each direction, we have collected 6×10^7 events for $x=40$, 2×10^7 events for $x=28$, and 1.8×10^7 events for $x=13$ in the total profile after background subtraction. The signal (CP maximum) to background ratio ranged from 20 to 1 for x

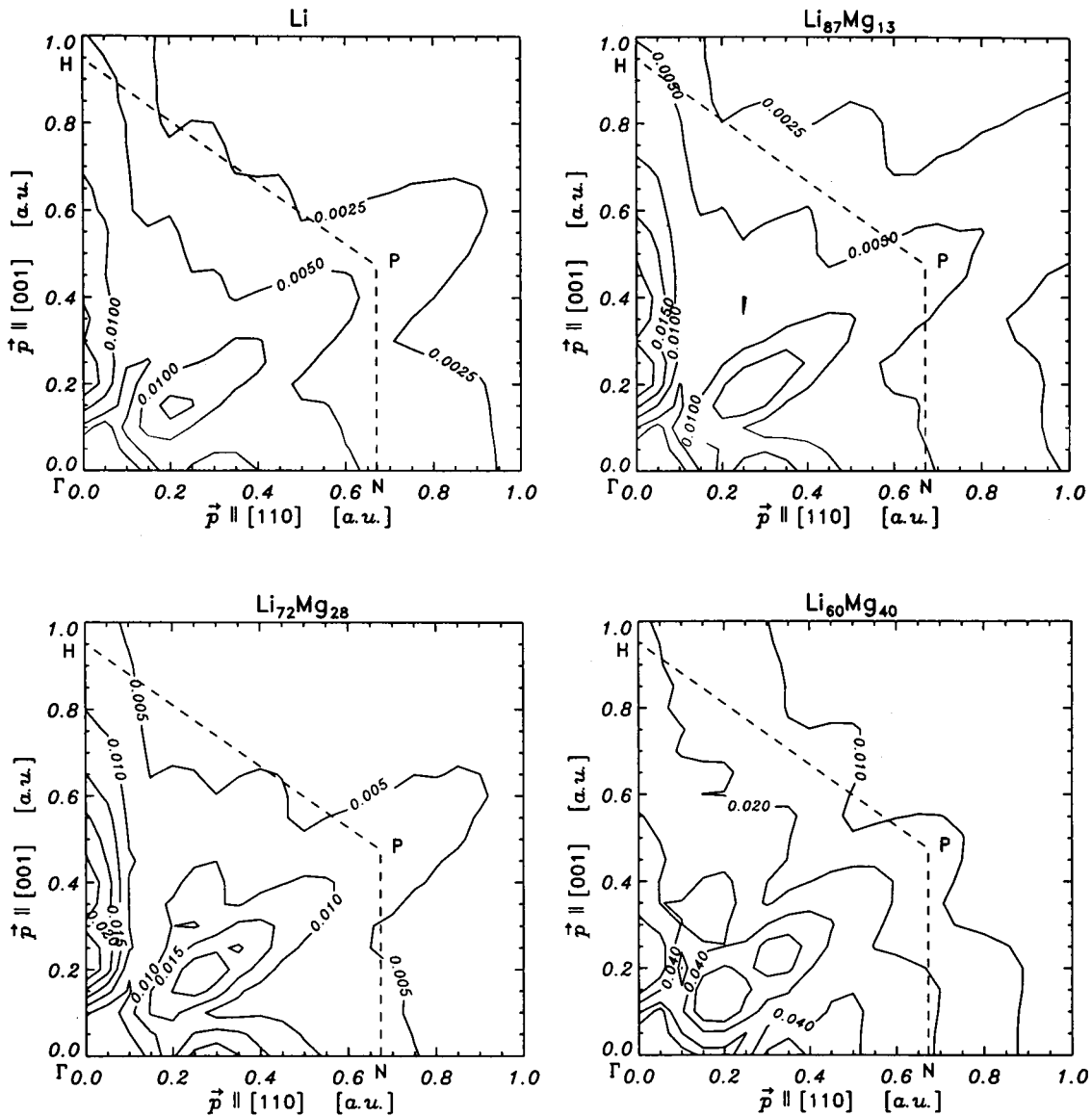


FIG. 7. Error map corresponding to Fig. 6, the level-line distances: 0.005 a.u.^{-3} for Li, $\text{Li}_{87}\text{Mg}_{13}$, and $\text{Li}_{72}\text{Mg}_{28}$; 0.02 a.u.^{-3} for $\text{Li}_{60}\text{Mg}_{40}$. Additionally, the level lines are plotted for 0.0025 a.u.^{-3} in the case of Li and $\text{Li}_{87}\text{Mg}_{13}$, and for 0.01 a.u.^{-3} in the case of $\text{Li}_{60}\text{Mg}_{40}$; dashed line is the BZ boundary.

$=40$ to 3 to 1 for $x=13$. This large difference is due to the very different effective scattering volumes. Experimental details of Compton measurements on pure Li, which are used as a reference in this work have already been published in Ref. 6. All these measurement were performed at the Compton beamline³⁹ of HASYLAB (Hamburger Synchronstrahlungs-LABor).

The procedure used for extracting the CP's $J(p_z)$ from the measured intensity distribution $I(x)$, where x is the linear position on the detector (image plates at KEK and Ge 200-strip detector at HASYLAB), has been described in detail in Ref. 4, including the necessary energy-dependent corrections (with respect to absorption, scaling, detector efficiency, analyzer crystal reflectivity, cross section, and multiple scattering) and the subtraction of a nonlinear background. The data processing described in Ref. 4 refers to the HASYLAB-data (pure Li). The KEK data (LiMg alloys) were processed the same way with one variation: The detector (image plate) ef-

iciency was experimentally determined along with the analyzer crystal reflectivity by measuring the intensity of various fluorescence lines in the relevant spectral range using the Cauchois analyzing system in combination with the image plate (energy-dependent efficiency) and using a Ge solid-state detector (nearly 100% efficiency independent on energy in that spectral range). The multiple-scattering contribution was calculated by means of a Monte Carlo simulation written by Sakai.⁴⁰ The relative portion of double scattering compared to single scattering was 2.7% for Li and 5% for the $\text{Li}_{60}\text{Mg}_{40}$ alloy in good agreement with calculations of Paatero and Halonen.⁴¹ The contribution of triple scattering could be neglected.

V. RESULTS AND DISCUSSION

A. Total Compton profiles, difference profiles

Figure 3 shows as an example the $\text{Li}_{60}\text{Mg}_{40}$ valence electron part of the CP for $\mathbf{q} \parallel [110]$ obtained by subtracting the

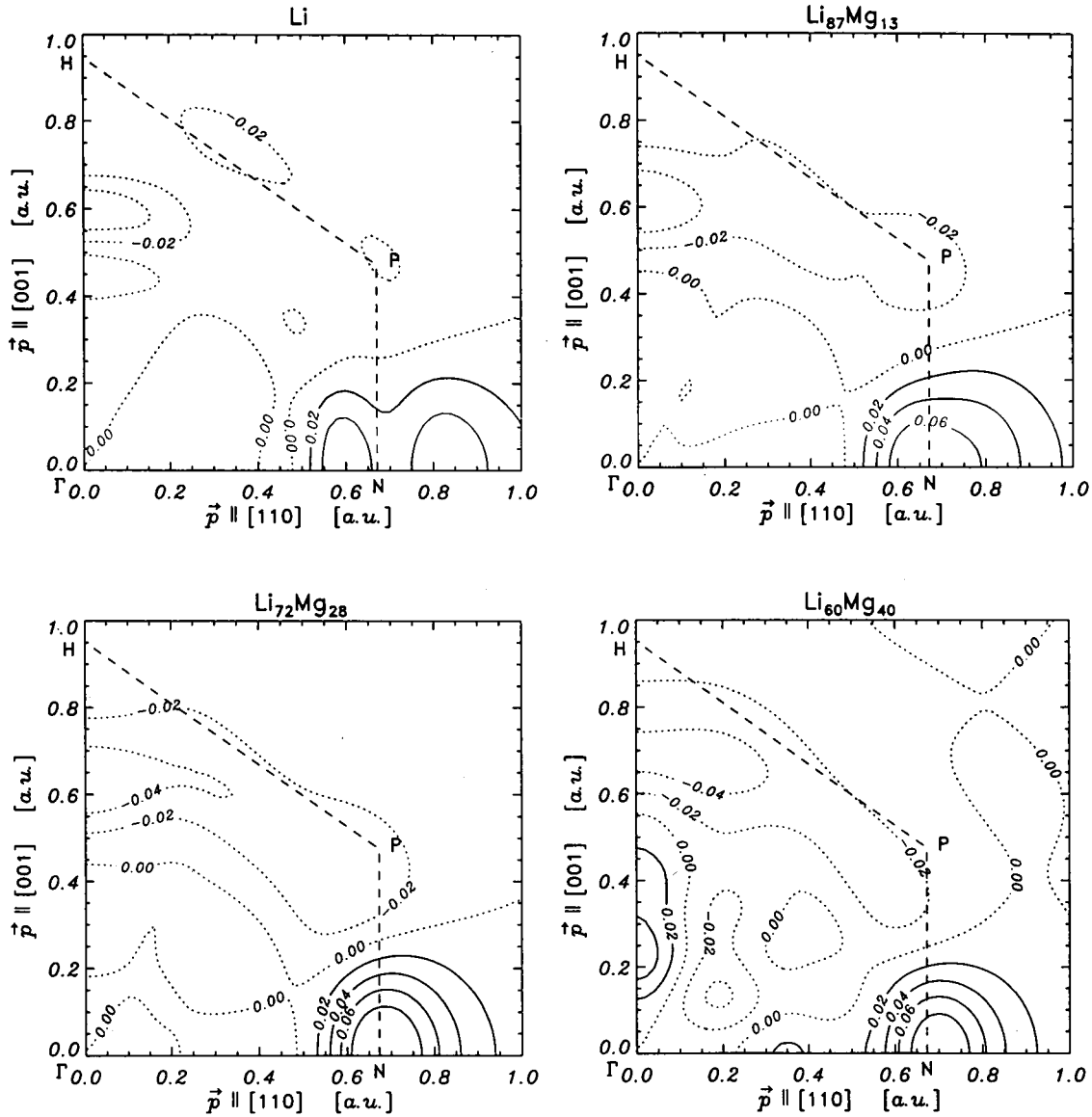


FIG. 8. Anisotropic parts $\Delta\rho(\mathbf{p})$ of the 3D valence-electron momentum densities reconstructed from the theoretical CP's in Li (KKR) and LiMg alloys (KKR-CPA) are shown in the (110) plane as level diagrams. Solid lines indicate positive values of $\Delta\rho(\mathbf{p})$; dotted lines indicate negative values of $\Delta\rho(\mathbf{p})$; level-line distance is 0.02 a.u.⁻³; dashed line is the BZ boundary.

core contribution⁴² from the total profile; the data points give the average for $p_z < 0$ and $p_z > 0$. The relative error at $p_z = 0$ is 0.6% and cannot be represented in form of an error bar. The corresponding KKR-LDA-CPA predictions are also plotted after convolution with a suitable Gaussian (0.16 a.u. FWHM) to reflect the momentum resolution of the experiment. As already mentioned, the Lam-Platzman-type correlation corrections³⁴ were not computed for alloys. In any event, the discrepancy in Fig. 3 is far from the experimental error, and is of roughly the same size in Li, where it has been shown⁴ (see also the discussion of Fig. 5 below) that this discrepancy is only reduced somewhat by an LDA-type correlation correction.³⁴ This statement applies to all LiMg-valence electron CP's. Interestingly, Kubo⁴³ has calculated correlation corrections within the GW scheme in Li and obtained a theoretical CP in substantial accord with the measurements. Several other recent attempts⁴⁴⁻⁴⁶ to study correlation effects on the momentum density are noteworthy.

More work is, however, needed for developing a practical scheme of wide applicability for incorporating such effects in materials. It has recently been proposed by Dugdale and Jarlborg⁴⁷ to explain the aforementioned discrepancy by a temperature effect. But it could be shown by Sternemann *et al.*⁴⁸ that in contrast to the predictions of Ref. 45 the Compton profile of Li is sharpened with rising temperature mainly due to the decreasing electron density.

Figure 4 shows the differences between the [110] and [100] directional CP's; results for other orientation differences are similar and not shown in the interest of brevity (see Ref. 4 for the case of Li). Although a reasonable overall accord between theory and experiment is evident, the amplitude of the oscillations in the experimental spectra is strongly attenuated compared to the theoretical predictions, especially in the low Mg concentration regime. Moreover, a number of discrepancies with respect to zero crossings can be seen. As discussed in Ref. 4, a part of these discrepancies can be

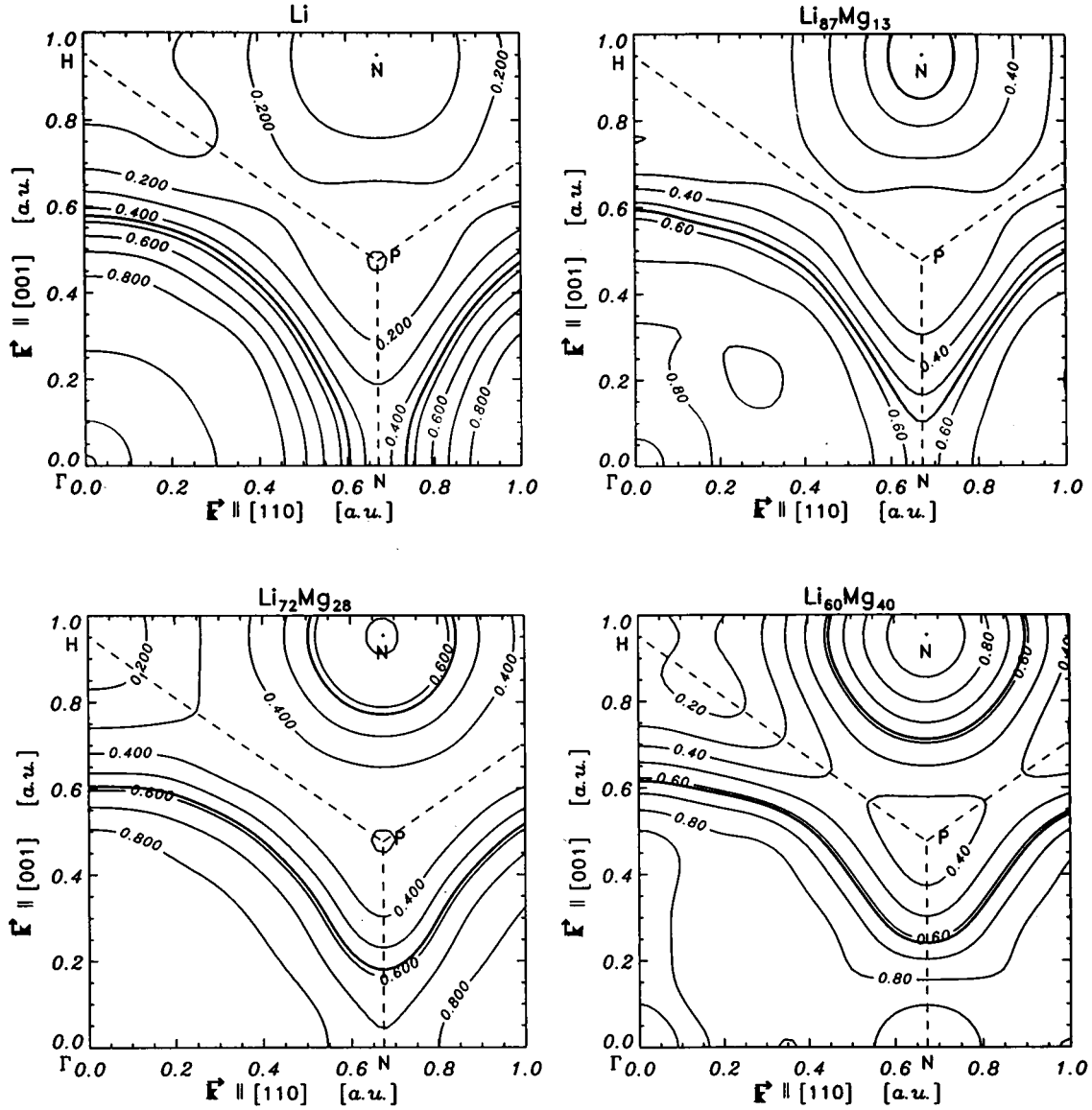


FIG. 9. Level diagrams of the occupation number density $N(\mathbf{k})$ in the repeated zone scheme in the ΓNPH plane for Li and LiMg alloys, 3D reconstructed from the experimental CP's. The level-line distance is 0.1 a.u.^{-3} . The trace of the Fermi surface, as defined via Eq. (10), is the bold solid line, the dashed line is the BZ boundary.

traced back to an isotropic smearing of the higher momentum components of the momentum density due to the excitation of plasmaron states during the Compton scattering process. This explanation finds support by plots of the difference between calculated and experimental CP's for different \mathbf{q} orientations in Fig. 5. As shown in Ref. 4, the \mathbf{q} -orientation dependent oscillating fine structure of these plots can likewise be attributed to a reduced contribution of higher momentum components seen in experiment compared to the theoretical predictions. Disregarding the aforementioned fine structure, the differences between theory and experiment in Fig. 5 are quite similar for various directional profiles. Also, the size and shape of the curves in Fig. 5 is similar for various Mg concentrations which indicates that correlation effects on the CP's in the LiMg alloys are insensitive to the electron/atom ratio. In order to demonstrate the role of the Lam-Platzman-correction,³⁴ this correction is plotted in Fig. 5 for the case of pure Li, so that one can see

that this correction cannot account completely for the difference between calculation and experiment.

B. 3D reconstructed momentum space densities

Using 11 CP's for Li and 12 CP's for each of the LiMg alloys, we have reconstructed the 3D momentum density $\rho(\mathbf{p})$ via the Fourier-Bessel method²⁶ described in detail in Ref. 4. The profiles were interpolated on an equidistant p_z scale ($\Delta p_z = 0.025 \text{ a.u.}$), and $B(z)$ values up to $z_{\max} = 30 \text{ a.u.}$ were taken into account. The value of z_{\max} was chosen such that $|B(z_{\max})| \approx \sigma_B$, where σ_B is the standard deviation of $B(z)$. In order to emphasize the physically interesting anisotropy of the momentum density, Fig. 6 gives the anisotropic part $\Delta\rho(\mathbf{p})$ of $\rho(\mathbf{p})$ in the ΓNPH plane in the form of a level diagram, where the $\Delta\rho(\mathbf{p})$ is obtained by subtracting the isotropic ($l=0$) part of an expansion of $\rho(\mathbf{p})$ into cubic harmonics; the corresponding error map⁴ of $\Delta\rho(\mathbf{p})$

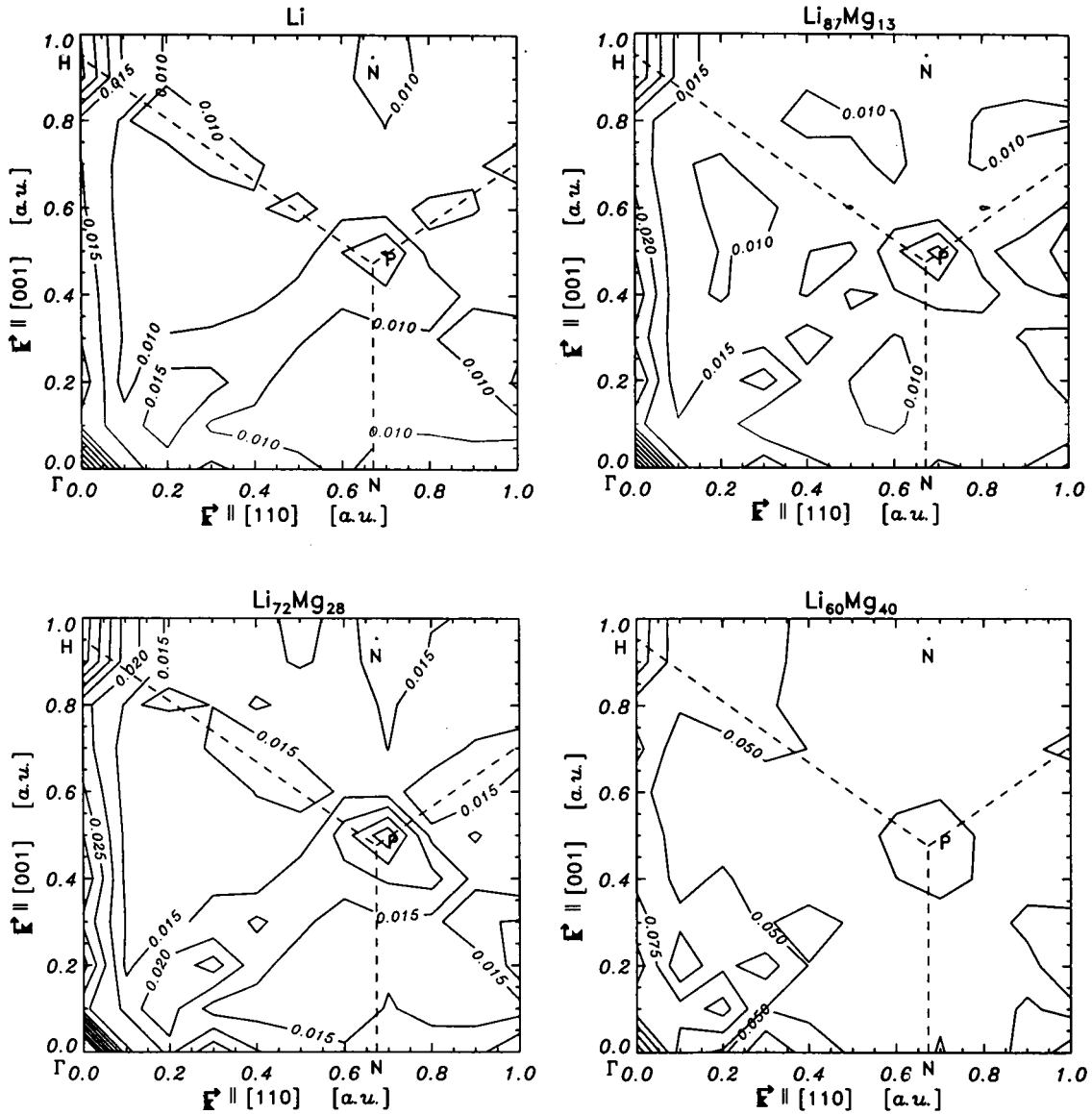


FIG. 10. Error map corresponding to Fig. 9. The level-line distance is 0.005 a.u.^{-3} (Li, $\text{Li}_{87}\text{Mg}_{13}$, $\text{Li}_{72}\text{Mg}_{28}$); 0.025 a.u.^{-3} ($\text{Li}_{60}\text{Mg}_{40}$). Dashed line is the BZ boundary.

is plotted in Fig. 7, where in the case of the LiMg alloys, beside the statistical error also the nonuniformity of the image plates was taken into account in the calculation⁴⁹ of the error of the experimentally reconstructed $\rho(\mathbf{p})$. One can easily verify that the only structures of $\Delta\rho(\mathbf{p})$, which are clearly beyond experimental error are (i) those around the 110 Brillouin-zone boundary near the N point (double-peak structure in the case of Li, which merges into a single peak for the LiMg alloys), (ii) the depression near p_F , which is around the ΓH direction in Li and $\text{Li}_{87}\text{Mg}_{13}$ but shifts to a position midway between ΓH and ΓP direction in alloys with higher Mg concentration, (iii) a broad peak around $p=0.4 \text{ a.u.}$ along ΓH in $\text{Li}_{60}\text{Mg}_{40}$, and (iv) a broad peak around $p=0.4 \text{ a.u.}$ along ΓP direction in $\text{Li}_{87}\text{Mg}_{13}$, associated with a depression around $p=0.7 \text{ a.u.}$ The strong oscillatory behavior of $\Delta\rho(\mathbf{p})$ between 0 and 0.4 a.u. , especially along ΓH , seems to be an artifact of the reconstruction procedure since the oscillation amplitudes are of the same order as the error in this region of momentum space, indicated in Fig. 7. As shown in Fig. 8,

the aforementioned structures (i) through (iii) in $\Delta\rho(\mathbf{p})$ are also found, when the 3D reconstruction procedure is applied to the calculated directional CP's (after including the experimental resolution) for the same 11(12) directions used for the reconstruction of the experimental data. The structure (i) in Li near the N point can be attributed to the bulge of the FS in the $[110]$ direction on the one hand (analyzed in more detail in Sec. V C below), and the strong higher momentum component induced by the \mathbf{G}_{110} th component of the crystal potential on the other. Both are separated by a momentum density gap, so that a double-peak structure occurs. With increasing Mg concentration, the FS makes contact with the 110 BZ boundary, causing the double-peaked structure to flow into a single peak shifted to somewhat higher momenta. The structure (ii) of $\Delta\rho(\mathbf{p})$ can be traced back to the reduction of the FS radius in $[100]$ and $[111]$ direction when compared with its mean value; this reduction is larger along the $[100]$ than the $[111]$ direction of Li and $\text{Li}_{87}\text{Mg}_{13}$ and of nearly equal size for higher Mg concentrations. Finally, fea-

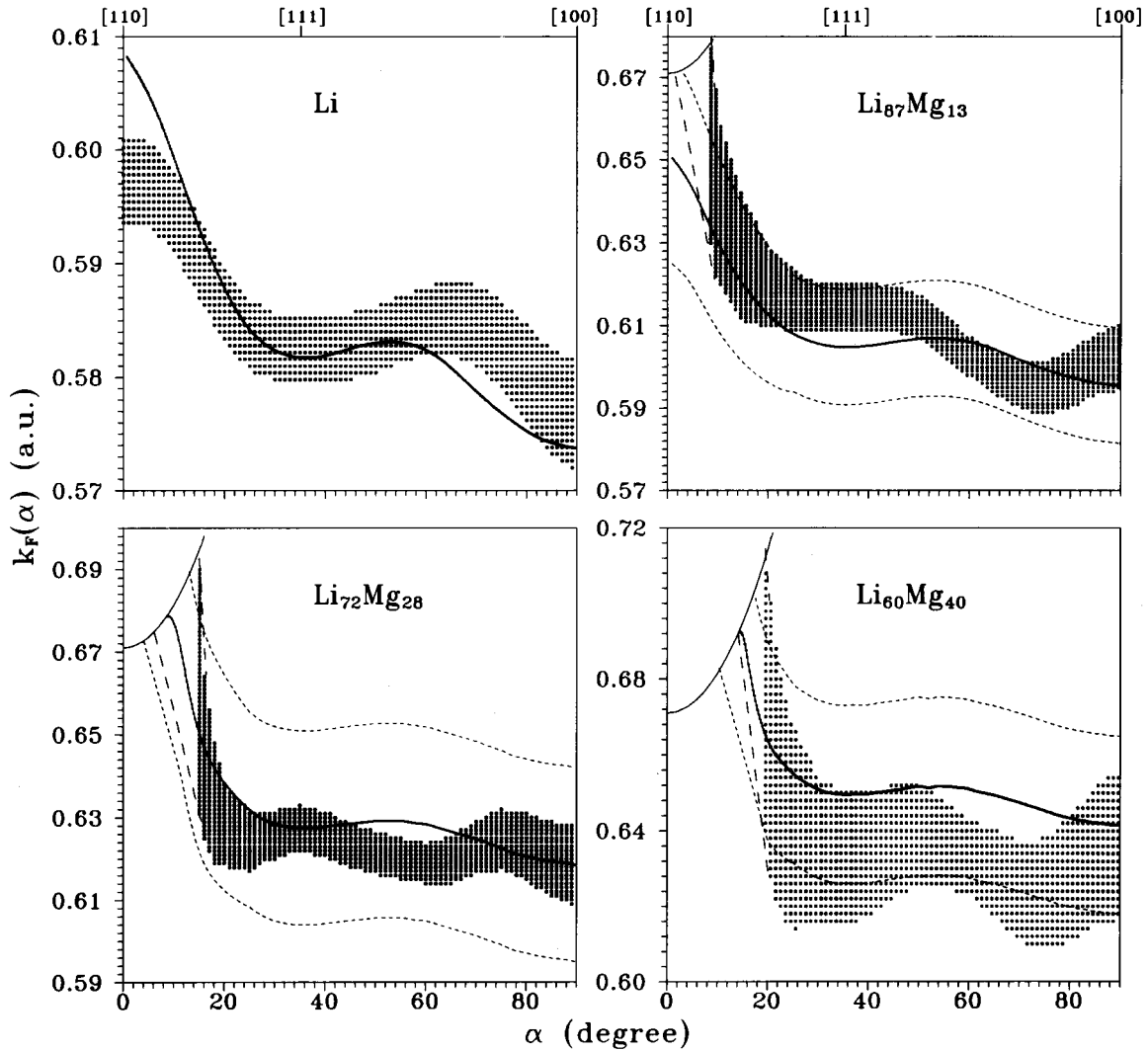


FIG. 11. Fermi radius $k_F(\alpha)$ in the ΓNPH plane, α is the angular distance of \mathbf{k}_F from the $[110]$ direction for Li and the LiMg alloys, as indicated in the insets. Screen-processed range: confidence range of the experiment. The long-dashed line is the extrapolated margins of the experimental confidence range. The bold solid line is the calculated [KKR (Li), KKR-CPA (LiMg alloys)]. The short dashed line is the range of FS smearing in the calculation due to disorder-induced scattering. The thin solid line is the distance of the 110-Brillouin-zone boundary from the Γ point as a function of α .

tures (iii) and (iv), which are only somewhat outside the error limits, presumably reflect the effect of redistribution of momentum density since they do not appear to be correlated to the FS topology. Notably, as seen by comparing Figs. 6 and 8 for the 13% alloy, structure (iv) is visible only in the experimental $\Delta\rho(\mathbf{p})$ but not in the corresponding theoretical plots.

C. 3D reconstruction of the occupation number density, Fermi-surface anisotropy

We have performed a 3D reconstruction of the occupation number density $N(\mathbf{k})$ in the repeated zone scheme via Eq. (8) by using the interpolated values of $B(\mathbf{R})$ obtained in the course of the $\rho(\mathbf{p})$ reconstruction. The results are presented in Fig. 9 for the ΓNPH plane. Figure 10 gives the corresponding error map.⁶ Assuming a single-sheeted FS, one reasonable approach⁵⁰ is to define the FS as the surface of constant $N(\mathbf{k})$, i.e.,

$$N(\mathbf{k}) = \text{const} = c, \quad (9)$$

where the constant c must be chosen to obtain the correct FS volume. This may be achieved, for example, in terms of the free-electron radius k_{F0} :

$$N(\mathbf{k}) \geq c, \quad \int d\mathbf{k} = (4/3)\pi k_{F0}^3, \quad (10)$$

where

$$k_{F0} = (3\pi^2 n_e)^{1/3} \quad (11)$$

and n_e is the valence-electron density.

The trace of the FS in the ΓNPH plane of the repeated zone scheme, determined by the preceding procedure is marked in Fig. 9 by bold lines. The FS radius $|\mathbf{k}_F|$ can then be measured along an arbitrary direction in the BZ, this ra-

dius must however be corrected as detailed in Ref. 6 by subtracting the FS anisotropy which appears even when the $N(\mathbf{k})$ reconstruction is performed using identical profiles. Figure 11 gives a plot of the FS radius $k_F(\alpha)$ where α is the angle between \mathbf{k}_F and the [110] direction in the ΓNPH plane. Thin solid lines give the corresponding distance from Γ to the 110-BZ boundary. The shaded region indicates the confidence range of the experimental $k_F(\alpha)$ values. The margins of this confidence range have been extended by long dashed lines to obtain an estimate of the FS neck radius on the 110-BZ boundary. The FS radii $k_F(\alpha)$ in a disordered alloy may be defined via the positions of the peak in the spectral density function $A(\mathbf{k}, E)$ along various directions in the BZ at $E = E_F$. These spectral peaks will in general possess finite widths $\Delta k_F(\alpha)$ reflecting the disorder scattering of states. In this sense, the alloy FS may be viewed as being “smeared” or “broadened.”⁵¹ The KKR-CPA results for $k_F(\alpha) \pm \Delta k_F(\alpha)$ are shown by the short-dashed lines to indicate the effective “width” of the alloy FS. Figure 11 shows that the FS in Li is less anisotropic than predicted by the present LDA based calculations (e.g., the calculated change between the [110] and [100] radii is substantially larger than the measurements). In the 13 at. % Mg alloy one sees a better accord as the shaded experimental region falls within the short dashed lines giving the width of the theoretical FS. This trend continues for the 28 at. % Mg alloy, but for the 40 at. % Mg alloy the computed radii appear to be systematically larger than the measurement.

The KKR-CPA size of the 110 neck (full circles connected by an interpolating curve) is compared with the present Compton (open squares) as well as the earlier¹⁶ 2D-ACAR experiments (filled triangles) in Fig. 12; the dashed lines again represent the disorder-induced FS width. The Compton experiment exhibits a contact with the 110-BZ boundary even in the 13 at. % Mg alloy contrary to the KKR-CPA computation, where only the upper limit of the disorder induced FS smearing produces a contact. But it can be seen in Fig. 12 that, also for higher Mg concentrations, both the neck diameter of our Compton measurements as well as the neck diameter of the 2D-ACAR results are always nearer to the upper limit of the theoretical disorder-induced smearing of the neck diameter. Therefore, the present results suggest that the LiMg alloy starts to develop a Fermi-surface neck at the 110-Brillouin-zone boundary already for Mg concentrations somewhat smaller than 13 at. %, slightly lower than the critical Mg concentration $x_c = 19-20$ found by both 1D-ACAR measurements¹³ and thermopower and resistivity measurements,¹⁷ and in total disagreement with the results of other experiments,¹⁹⁻²¹ listed in the Introduction, which all deduce x_c larger than 30. Unfortunately, no 2D-ACAR results¹⁶ for $x < 28$ were presented. Nevertheless, the good agreement between the Compton and the 2D-ACAR results for higher Mg concentration is striking and seems to indicate that the KKR-CPA underestimates the neck width of the LiMg alloys.

D. Second derivative of the Compton profiles

FS-induced discontinuities in the momentum density can be highlighted via the second derivative $d^2J(p_z)/dp_z^2$ of the CP since such discontinuities will, in general, appear as

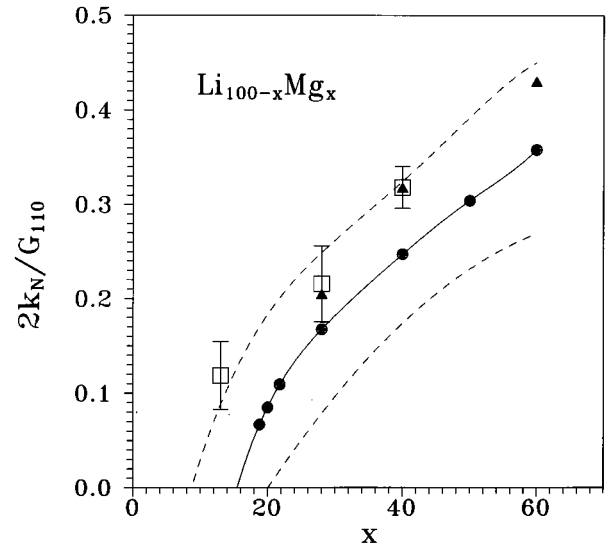


FIG. 12. Fermi-surface neck diameter on the 110-BZ boundary in units of the reciprocal-lattice vector \mathbf{G}_{110} as a function of the Mg concentration. Open squares are the present Compton experiment. Triangles are the 2D-ACAR experiment (Ref. 16). Filled circles connected by an interpolating line are the KKR-CPA calculation. Dashed lines mark the range of smearing of the theoretical neck diameter due to disorder-induced scattering.

peaks in $d^2J(p_z)/dp_z^2$. In analyzing structure in $d^2J(p_z)/dp_z^2$, it is important, however, to bear in mind the complex interplay of effects of experimental resolution, electron correlation, lattice potential, and in the case of an alloy, of disorder scattering of states. Note first that for noninteracting free electrons, $d^2J(p_z)/dp_z^2$ will consist of a δ -function-like peak which sits on top of a step function, both located at k_F ; the inclusion of experimental resolution will then yield an asymmetric peak. Disorder in alloys will cause further broadening whose shape is Lorentzian at least for weakly scattering cases. Electron correlation not only reduces the size of the FS breaks and thus the weight of the associated δ function in $d^2J(p_z)/dp_z^2$,³⁴ but also rounds momentum density in the vicinity of k_F . This rounding may be roughly thought as a rather broad component (width of the order of the Fermi momentum) to the FS peak in $d^2J(p_z)/dp_z^2$; note that this additional structure is not resolution limited as in the case for the peak arising from the FS discontinuity. Finally, the effect of the periodic lattice potential is somewhat similar to that of correlation in that the FS breaks are reduced, and the momentum density is rounded, although additional breaks in this case will generally appear at Umklapp momenta. One should bear these remarks in mind for proper analysis of the structure in $d^2J(p_z)/dp_z^2$.

In discussing Fig. 13, it is helpful to focus first on the theoretical spectra. The position of all FS peaks are seen to move to higher momenta with increasing Mg concentration as the FS grows in size consistent with the results of Fig. 11. This is true of the (110) peak position as well, except that in this case the contact with the BZ boundary occurs around x approximately 18% (see Fig. 12); the (110) peak is thus essentially pinned to the zone boundary for greater Mg concentrations although some shifts in the (110) peak position still continue to take place due to subtle spectral weight changes

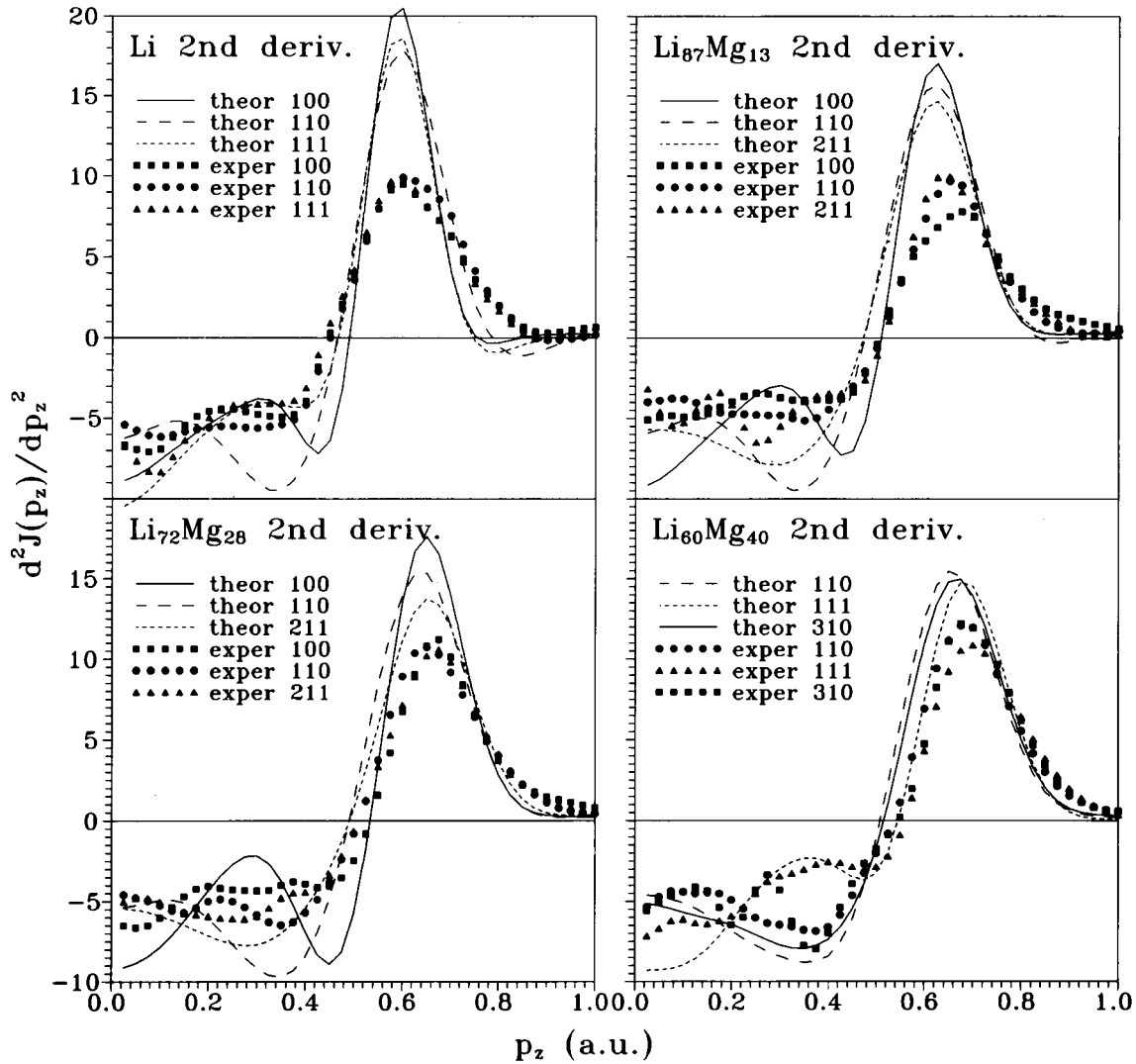


FIG. 13. Second derivative of theoretical (lines) and experimental (points) directional CP's of Li and LiMg alloys. The relation of line and point styles to the \mathbf{q} directions is given in the insets. Note that the (100) directional CP for $\text{Li}_{60}\text{Mg}_{40}$ was not measured (see Fig. 1).

in the underlying momentum density. All peaks in the alloys are of course broadened compared to Li due to the effect of disorder smearing.

An examination of Fig. 13 indicates that the positions of the FS peaks in the experimental spectra move to higher momenta with increasing Mg concentration in much the same way as the corresponding theoretical predictions. However, the experimental (110) peak position shows a substantially larger movement in going from Li to the 13% Mg alloy. This is to be expected since, as already noted above, the KKR-CPA predicts the appearance of the (110) neck at a higher Mg critical concentration than the present measurements.

We emphasize that although the heights of the theoretical FS peaks in Fig. 13 decrease systematically with increasing Mg content due to disorder smearing, the experimental peak heights are more or less independent of the alloy composition. In the 40% Mg alloy, theory and experiment seem to be in reasonable accord in this respect even though in Li this is far from being the case. This is surprising because we do not expect electron correlation effects to change much as r_s changes from 3.26 in Li to 2.91 in the 40% Mg alloy, i.e., by

only 11%. Recall from Fig. 5 that the overall shape and amplitude of the difference between the computed (LDA based) and measured CP's is quite the same in all alloys. If one makes the reasonable assumption that the discrepancy of Fig. 5 originates in the electron correlation effects beyond the LDA missing in the computations, it follows that such effects are fairly insensitive to Mg concentration, contrary to the results of Fig. 13 where the discrepancy is quite large in Li but not in $\text{Li}_{60}\text{Mg}_{40}$. In fact, the order of magnitude of the discrepancy for the 40% Mg alloy in Fig. 13 could be explained straightforwardly via Lam-Platzman-type correction within the LDA framework (not included in the present computations in alloys). It is important to establish whether Li or $\text{Li}_{60}\text{Mg}_{40}$ in Fig. 13 is more representative of the behavior of the momentum density around FS breaks in metals. Further investigation of this issue should prove worthwhile.

VI. CONCLUSIONS

(1) As in the case of pure Li,^{3,4} the values of all measured total valence CP's of LiMg alloys are smaller at $p_z=0$, and larger values at $p \approx k_F$ compared to the corresponding KKR-

CPA–LDA predictions. The inclusion of the so-called Lam-Platzman correction³³ to the theoretical CP's within the LDA framework is expected only to reduce the size of this discrepancy somewhat but not eliminate it. Much like the earlier study of Li,⁴ these results indicate the importance of plasmaron states in the Compton scattering process, and suggest that the FS break in LiMg alloys is strongly reduced compared to the jellium computations.³⁴ Moreover, the amplitudes of oscillations in the measured directional differences are smaller than the corresponding computations in alloys investigated, indicating that the contributions of umklapp FS's to the CP's is smaller than KKR–CPA predictions, especially in the low Mg concentration regime.

(2) An analysis of the anisotropic part of the reconstructed 3D-momentum density in Li and LiMg alloys gives strong evidence for the presence of a FS neck [around the (110) BZ boundary] whose size grows with increasing Mg concentration.

(3) The reconstructed 3D occupation number density of Li and LiMg alloys enables a determination of the radii of the aforementioned (110) FS necks. The experimental neck radii are found to be systematically higher than the KKR–CPA results, but in accord with the corresponding ACAR measurements.^{15,16} The present Compton data indicates the presence of the neck even in the 13 at. % Mg alloy, whereas the KKR–CPA predicts the (110) neck to first appear at the critical concentration of about 18 at. % Mg.

(4) The FS related peaks in the second derivative

$d^2J(p_z)/dp_z^2$ of the CP's move much as expected to higher momenta with increasing Mg content reflecting the growth of the FS dimensions. The KKR–CPA predicts the heights of the FS peaks in $d^2J(p_z)/dp_z^2$ to decrease as Mg concentration increase due to disorder scattering effects. The corresponding measured peaks however are nearly unchanged in height so that theory and experiment are curiously in reasonable accord for the 40 at. % Mg alloy even though this is far from being the case in Li. This puzzling result bears further investigation since it hints that the behavior of momentum density in Li may be idiosyncratic and not representative of metals more generally.

ACKNOWLEDGMENTS

We acknowledge important conversations with Bernardo Barbiellini and Peter Mijnarends. The CP measurements were performed with the approval of the Photon Factory Advisory Committee, Proposal No. 92-G257 and 94-G351. This work was funded by the German Federal Ministry of research and Technology under Contract No. 05 SPEAXB 6. The work at Northeastern University is supported under the U.S. Department of Energy Contract No. W-31-109-ENG-38, and benefitted from the allocation of supercomputer time at NERSC and the NPACI supercomputer centers, and a travel grant from NATO. G.S. thanks the Konrad Adenauer Stiftung for financial support.

*Present address: Facultad de Matematica, Astronomia y Fisica, Universidad Nacional de Cordoba, 5000 Cordoba, Argentina.

†Present address: Academy of Mining and Metallurgy, Institute of Physics and Nuclear Techniques, Krakow, Poland.

¹W. E. Freeth and G. V. Raynor, *J. Inst. Met.* **82**, 575 (1953).

²F. H. Herbstein and B. L. Averbach, *Acta Metall.* **4**, 407 (1956).

³Y. Sakurai, V. Tanaka, A. Bansil, S. Kaprzyk, A. T. Stewart, Y. Nagashima, T. Hyodo, S. Nanao, H. Kawata, and N. Shiotani, *Phys. Rev. Lett.* **74**, 2252 (1995).

⁴W. Schülke, G. Stutz, F. Wohlert, and A. Kaprolat, *Phys. Rev. B* **54**, 14 381 (1996).

⁵H. G. Smith, *Phys. Rev. Lett.* **58**, 1228 (1987).

⁶D. L. Randles and M. Springford, *J. Phys. F* **6**, 1827 (1976).

⁷See, for a review, W. Schülke, in *Handbook on Synchrotron Radiation*, edited by G. Brown and D. E. Moncton (Elsevier Science, Amsterdam, 1991), pp. 565–637.

⁸See, for a review, S. Berko, in *Positron Solid State Physics*, edited by W. Brand and A. Dupasquier (North-Holland, Amsterdam, 1983), pp. 64–145.

⁹D. G. Lock, V. H. C. Crisp, and R. N. West, *J. Phys. F* **3**, 561 (1973).

¹⁰W. Schülke, *Phys. Status Solidi B* **82**, 229 (1977); **80**, K67 (1977).

¹¹P. Kubica, B. T. A. McKee, A. T. Stewart, and M. J. Stott, *Phys. Rev. B* **11**, 11 (1975).

¹²M. J. Stott and P. Kubica, *Phys. Rev. B* **11**, 1 (1975).

¹³A. T. Stewart, *Phys. Rev.* **133**, A1651 (1964).

¹⁴O. Brümmer, K. Berndt, and W. Schülke (unpublished); K. Berndt and O. Brümmer, *Phys. Status Solidi B* **78**, 659 (1976).

¹⁵W. Triftshäuser, A. Eckert, G. Kögel, and P. Sperr, *Mater. Sci. Forum* **105-110**, 501 (1992).

¹⁶S. S. Rajput, R. Prasad, R. M. Singru, W. Triftshäuser, A. Eckert, G. Kögel, S. Kaprzyk, and A. Bansil, *J. Phys.: Condens. Matter* **5**, 6419 (1993).

¹⁷V. S. Egorov and A. N. Fedorov, *Zh. Eksp. Teor. Fiz.* **85**, 1647 (1983) [*Sov. Phys. JETP* **58**, 959 (1983)].

¹⁸V. G. Vaks, A. V. Trefilov, and S. V. Fomichev, *Zh. Eksp. Teor. Fiz.* **80**, 1613 (1981) [*Sov. Phys. JETP* **53**, 830 (1981)].

¹⁹M. Ide, *J. Phys. Soc. Jpn.* **30**, 1352 (1971).

²⁰A. G. Mathewson and H. P. Myers, *J. Phys. F* **3**, 623 (1973).

²¹G. F. Lynch, M. J. Stott, and A. R. Williams, *Solid State Commun.* **13**, 1675 (1973).

²²P. Eisenberger and P. M. Platzman, *Phys. Rev. A* **2**, 415 (1970).

²³R. Ribberfors, *Phys. Rev. B* **12**, 3136 (1975).

²⁴B. I. Lundqvist and C. Lyden, *Phys. Rev. B* **4**, 3360 (1971).

²⁵P. Pattison, W. Weyrich, and B. Williams, *Solid State Commun.* **21**, 967 (1977).

²⁶N. K. Hansen, *Reconstruction of the EMD from a Set of Directional Compton Profiles* (Hahn Meitner Institut, Berlin, 1980), Rep. HMI B 342.

²⁷A. Bansil, S. Kaprzyk, and J. Tobo, in *Application of Multiple Scattering Theory to Materials Science*, edited by W. H. Butler *et al.*, MRS Symposia Proceedings No. 253 (Materials Research Society, Pittsburgh, 1992), p. 505.

²⁸S. Kaprzyk and A. Bansil, *Phys. Rev. B* **42**, 7358 (1990); A. Bansil and S. Kaprzyk, *Phys. Rev. B* **43**, 10335 (1991).

²⁹S. Kaprzyk, *Acta Phys. Pol. A* **91**, 135 (1997).

³⁰P. E. Mijnarends and A. Bansil, *Phys. Rev. B* **13**, 2381 (1976).

³¹A. Bansil, R. S. Rao, P. E. Mijnarends, and L. Schwartz, *Phys. Rev. B* **23**, 3608 (1981).

³²A. Bansil, *Z. Naturforsch. Teil A* **48A**, 165 (1993).

³³U. von Barth and L. Hedin, *J. Phys. C* **5**, 1629 (1972); A. K.

- Rajagopal and J. Callaway, *Phys. Rev. B* **7**, 1912 (1973).
- ³⁴L. Lam and P. M. Platzman, *Phys. Rev. B* **9**, 5122 (1974).
- ³⁵H. Kawata, M. Sato, T. Iwazumi, M. Ando, N. Sakai, M. Ito, Y. Tanaka, N. Shiotani, F. Itoh, H. Sakurai, Y. Sakurai, Y. Watanabe, and S. Nanao, *Rev. Sci. Instrum.* **62**, 2109 (1991).
- ³⁶Y. Sakurai, M. Ito, Y. Tanaka, N. Sakai, T. Iwazumi, H. Kawata, M. Ando, and N. Shiotani, *Rev. Sci. Instrum.* **63**, 1190 (1992).
- ³⁷J. Miyahara, K. Takahashi, Y. Amemiya, N. Kamiya, and Y. Satow, *Nucl. Instrum. Methods Phys. Res. A* **246**, 572 (1986).
- ³⁸M. Ito and Y. Amemiya, *Nucl. Instrum. Methods Phys. Res. A* **310**, 369 (1991).
- ³⁹A. Berthold, S. Mourikis, J. R. Schmitz, W. Schülke, and H. Schulte-Schrepping, *Nucl. Instrum. Methods Phys. Res. A* **317**, 373 (1992).
- ⁴⁰N. Sakai, *J. Phys. Soc. Jpn.* **56**, 2477 (1987).
- ⁴¹P. Paatero and V. Halonen, *Nucl. Instrum. Methods* **135**, 537 (1976).
- ⁴²F. Biggs, L. B. Mendelsohn, and J. B. Mann, *At. Data Nucl. Data Tables* **16**, 201 (1975).
- ⁴³Y. Kubo, *J. Phys. Soc. Jpn.* **66**, 2236 (1997).
- ⁴⁴B. Kralik, P. Delaney, and S. G. Louie, *Phys. Rev. Lett.* **80**, 4253 (1998).
- ⁴⁵C. Filippi and D. M. Ceperley, *Phys. Rev. B* **59**, 7907 (1999).
- ⁴⁶B. Barbiellini, cond-mat/9804145 (unpublished).
- ⁴⁷S. B. Dugdale and T. Jarlborg, *Solid State Commun.* **105**, 283 (1998).
- ⁴⁸C. Sternemann, G. Döring, C. Wittkop, W. Schülke, A. Shukla, T. Buslaps, and P. Suortti, *J. Phys. Chem. Solids* (to be published).
- ⁴⁹G. Stutz, Ph.D. thesis, Dortmund University, 1995.
- ⁵⁰The FS could perhaps be more naturally defined via the maximum gradient of the occupation number density $N(\mathbf{k})$. We have carried out such simulations extensively, and find that the FS defined in this manner lies within the experimental error bars of the result obtained on the basis of Eqs. (9)–(11) insofar as the anisotropy of the FS is concerned. However, the volume of the FS defined through such a gradient scheme deviates in some cases from the proper (free-electron) volume by somewhat more than allowed for through the statistical error in $N(\mathbf{k})$, possibly due to small truncation-induced oscillations. Therefore, we decided to define the FS in all cases via Eqs. (9)–(11). We emphasize in particular that our statement that the 13 at. % Mg alloy possesses a (110) neck is independent of which of the two aforementioned methods is used to determine the FS.
- ⁵¹A. Bansil, *Z. Naturforsch. Teil A* **48a**, 165 (1993).